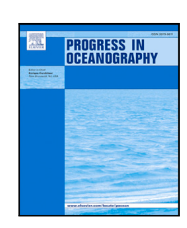
ELSEVIER

Contents lists available at ScienceDirect

Progress in Oceanography

journal homepage: www.elsevier.com/locate/pocean



The Rio Grande Rise circulation: Dynamics of an internal tide conversion hotspot in the Southwestern Atlantic

Pedro W.M. Souza-Neto ^{a,*}, Ilson C.A. da Silveira ^a, Cesar B. Rocha ^{a,b}, Cauê Z. Lazaneo ^{a,c}, Paulo H.R. Calil ^d

- a Instituto Oceanográfico, Universidade de São Paulo, São Paulo, 05508-120, Brazil
- b Department of Marine Sciences, University of Connecticut, Groton, 06340, United States
- ^c Department of Earth System Science, Stanford University, Stanford, 94305, United States
- d Institute of Carbon Cycles, Helmholtz-Zentrum Hereon, Geesthacht, 21502, Germany

ARTICLE INFO

Keywords: Rio Grande Rise Cruzeiro do Sul Rift Internal tides Tidal beams Bottom currents Anticyclonic circulations Tidal rectification

ABSTRACT

The Rio Grande Rise (RGR) is a plateau located at 31°S in the Southwestern Atlantic, rising from 5916 m up to 161 m below the sea level. The RGR is an important site for future mining of Fe-Mn crusts and can lead to an expansion of Brazil's Exclusive Economic Zone. The Cruzeiro do Sul Rift (CSR) fault cuts through the RGR from southeast to northwest. In this study we characterize the RGR circulation, showing that M2 tides are the main source of variability in the region, with an amplitude that can reach 0.3 m s⁻¹, larger than the mean flow. These M2 tides are dominated by the baroclinic component and intensified near the bottom. The generation of M2 internal tides occurs mainly in the CSR slopes, with most energy converted from the barotropic tide being radiated away in the form of tidal beams. In addition, the impingement of the mean southern South Equatorial Current and tidal rectification generates anticyclonic circulations around the RGR peaks, with the latter mechanism being responsible for a bottom intensified anticyclonic circulation of 0.2 m s⁻¹. Finally, our results reveal that the RGR is a hotspot of internal tide generation in the Southwestern Atlantic.

1. Introduction

The Rio Grande Rise (RGR) is an aseismic oceanic elevation in the South Atlantic, between 28°S–35°S and 29°W–39°W (Fig. 1a). It is located approximately 1300 km east of the Brazilian coast (Cavalcanti et al., 2015) and is the largest plateau in the South Atlantic, having approximately 3000 km² (Praxedes et al., 2019). The feature extends from 5916 m up to 161 m depth (Montserrat et al., 2019).

The RGR can be divided into two portions (Cavalcanti et al., 2015), the RGR West (RGRw) and the RGR East (RGRe, Fig. 1a). The area of interest of this study is the RGRw (Fig. 1b) hereafter RGR. The RGR is cut by a fracture zone oriented in the southeast–northwest direction (Fig. 1b). This fault is called Cruzeiro do Sul Rift (CSR), which is about 30 km wide and over 2 km deep (Praxedes et al., 2019).

The RGR has a diverse environment that is composed of different bottom substrates (Figure 61 in Lisniowski, 2020). Two types of plates are found on the top of the RGR: the carbonatic plates, which may contain dunes (Lisniowski et al., 2017) and the Fe-Mn crusted plates (Benites et al., 2020, 2021, 2023). The Fe-Mn crusted plates were observed up to 1500 m (Cavalcanti et al., 2015; Lisniowski, 2020) and according to Yeo et al. (2019), currents stronger than $0.2 \, \mathrm{m \, s^{-1}}$

may be able to erode the surface of Fe-Mn crusts. Due to the mining potential of polymetallic crusts, there is a substantial geopolitical and economic interest in the region, related to its proximity to the Brazilian Exclusive Economic Zone and the presence of crusts rich in rare metals (Silva, 2021). The Fe-Mn crusts are essential for the high-technology industry (Hein et al., 2013; Montserrat et al., 2019).

The large-scale circulation in the region is characterized by the presence of the westward-flowing southern South Equatorial Current (sSEC), one of the branches of the South Equatorial Current (Peterson and Stramma, 1991; Stramma and England, 1999; Rodrigues et al., 2007; Luko et al., 2021). Luko et al. (2021) showed from altimetry and a set of four reanalyses that the sSEC itself is a multi-banded jet. Indeed, the sSEC consists of six branches, with the southernmost branch at 30°S, the same latitude as the RGR (Fig. 1). The 30°S branch extends from the surface down to 2500 m, with the core depth ranging between 287–570 m. This branch impinges on the RGR and bifurcates, going around the rise.

The hydrodynamics within submerged rifts, ridges, and rises is still an area of active research due to, for example, its implications in the larval dispersion patterns (Vic et al., 2018) and hydrodynamic control

E-mail address: pedro.walfir.neto@alumni.usp.br (P.W.M. Souza-Neto).

^{*} Corresponding author.

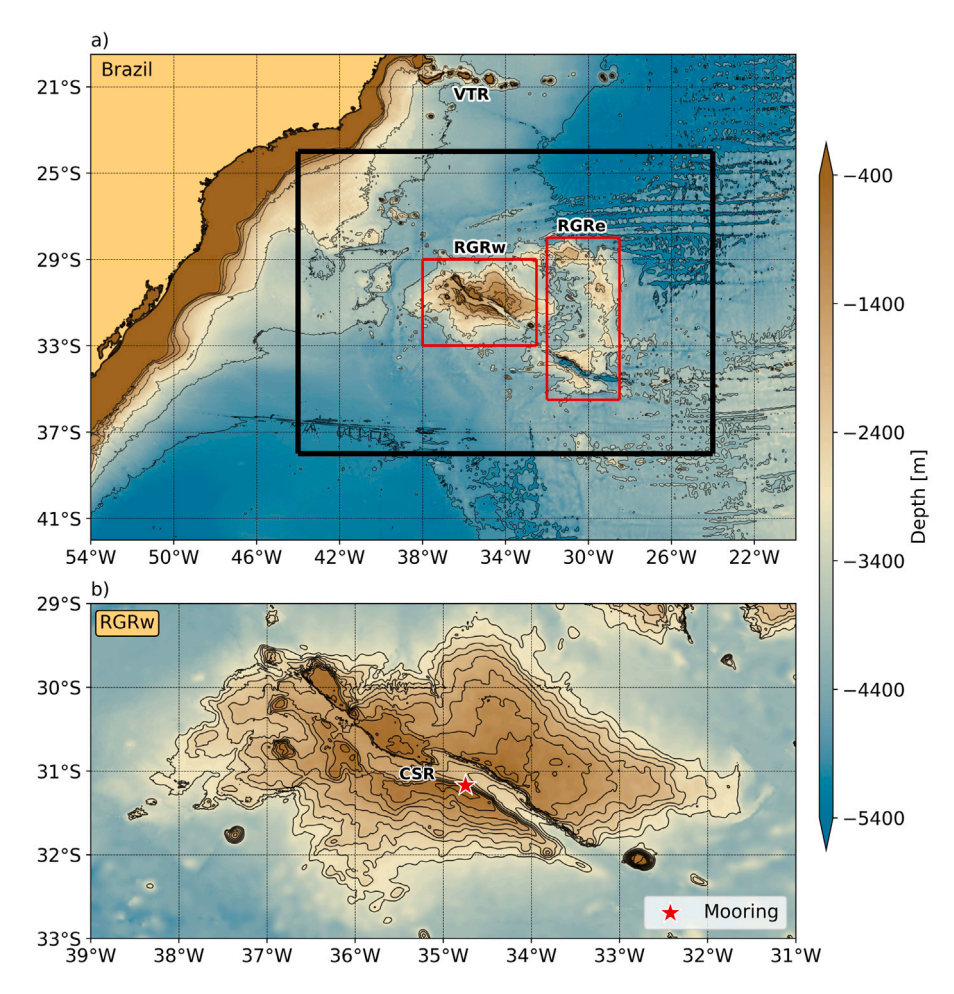


Fig. 1. (a) The bathymetry of the Southwestern Atlantic. The map highlights the main topographical features: Vitória Trindade Ridge (VTR), and marked by the red rectangles the Rio Grande Elevation (RGR) that can be divided into RGR West (RGRw) and RGR East (RGRe). The black rectangle shows the numerical simulation domain. (b) Bathymetric map of the RGRw. The map highlights that the Cruzeiro do Sul Rift (CSR) cuts the entire RGRw in the northwest–southeast direction. The red star marks the position of the current meter mooring deployed at the 1250 m isobath on the CSR south slope. Bathymetry data obtained from GEneral Bathymetric Chart of the Oceans (GEBCO) (GEBCO Compilation Group, 2021).

of Fe-Mn crust outcrops (Yeo et al., 2019). Very little is known about the dynamics and spatial–temporal variability of the circulation in the RGR. The only work focused on characterizing the circulation in the RGR on a local scale is the study by Harlamov et al. (2015), who found mean velocities at the top of the RGR on the order of 0.1 m s $^{-1}$, with peaks reaching 0.5 m s $^{-1}$. The authors stated that the hydrodynamics in the region is largely tide-driven.

The interaction between barotropic tides and the topography in a stratified ocean gives rise to baroclinic tides, also known as internal tides. Regions with an intense generation of internal tides, such as Monterey Bay, are known for presenting intense near-bottom tidal currents (Carter, 2010). Internal tides encompass a large interval of horizontal and vertical scales. On one hand, low-mode internal tides can propagate for long distances from their location of formation, propagating through thousands of kilometers. The breaking of these internal tides can strengthen the far-field background mixing. On the other hand, high-mode internal tides do not propagate for long distances as low-mode internal tides and form tidal beams, they are susceptible to local breaking due to wave-wave interactions (Nikurashin and Legg, 2011). Since high-mode internal tides break close to the origin site, they enhance the mixing locally. According to Vic et al. (2019), high-mode internal tides account for more than 50% of the ocean's internal tide generation, breaking, and mixing.

In the southwestern Atlantic Ocean, Paiva et al. (2018) estimated the mode-1 baroclinic M2 energy fluxes using satellite altimetry. They highlighted that just from the surface signature, the Vitória Trindade

Ridge (VTR - 20.5°S, Fig. 1a) is the main site of the formation of internal tides. Two main beams are generated in the VTR, one propagates northward with an energy flux of $1\,\mathrm{kW}\,\mathrm{m}^{-1}$ and the other one southward with fluxes spanning from 2 to $3\,\mathrm{kW}\,\mathrm{m}^{-1}$. The southward propagating beam reaches 30°S, adjacent to the RGR. The authors also depicted that some beams are observed propagating from the RGR, however, those beams do not propagate for long distances, being constrained by the bathymetry. Further south, Pereira and Castro (2007) evidences the presence of prominent M2 internal tides at 24°S in the Brazilian continental shelf with fluxes of $10\,\mathrm{W}\,\mathrm{m}^{-1}$, 2 orders of magnitude smaller than those observed in the VTR. Also, the Mid-Atlantic Ridge is an internal tide hotspot, as reported by Zilberman et al. (2009), with fluxes in the order of $1\,\mathrm{kW}\,\mathrm{m}^{-1}$.

Another process that is topographically induced is the formation of anticyclonic circulation around the seamount summit can be found around many topographic features, such as the Le Danois Bank (González-Pola et al., 2012), Condor seamount (Bashmachnikov et al., 2013), Caiwei Guyot (Guo et al., 2020) and the Axial Seamount (Xu and Lavelle, 2017). The main mechanisms responsible for generating this type of circulation around seamounts are the presence of an impinging mean flow and/or the rectification of oscillatory flows.

The presence of an impinging mean flow allows the formation of a Taylor column when the stratification is weak and the anticyclonic circulation extends to the surface. A Taylor cap is formed when the stratification is stronger and constrains the anticyclonic circulation to the seamount summit. This process is a consequence of potential vorticity conservation when steady and stratified currents pass over a ridge or seamount (Chapman and Haidvogel, 1992; Xu and Lavelle, 2017). The rectification of oscillatory flows occurs mainly with tidal flows. This process happens due to the non-linear interaction between the tidal flow and the steep topography, allowing the bottom friction and the topographic acceleration to develop an on-slope transport (Haidvogel et al., 1993; Chen and Beardsley, 1995; Guo et al., 2020).

In this study, we analyze the role of tides in the Rio Grande Rise hydrodynamics. To address this topic we seek an understanding of (i) the vertical and horizontal variability in the RGR domain, (ii) the generation radiation and dissipation of the baroclinic tides, and (iii) the non-linear interaction between tides and topography and the effect on the RGR circulation.

2. Data set

To investigate the RGR circulation and the associated superinertial variability we analyze velocity time series from a current meter mooring from the Marine-Etech Experiment (Jovane et al., 2019). The mooring was located at 31.172°S and 34.748°W (Fig. 1b), placed on the CSR slope for approximately 1 year and two months, ranging from 02/04/2018 to 04/12/2019, with a temporal resolution of 20 min. The mooring consists of two Teledyne RDI WorkHorse 300 kHz Acoustic Doppler Current Profilers (ADCP) deployed in opposite directions measuring with 2 m vertical resolution. The ADCPs were approximately 20 m from the bottom (1250 m depth). We also use a regional numerical simulation to achieve a higher temporal and spatial resolution.

ADCP velocities were motion corrected using pitch and roll measured internally by a gyro. The Integrated Marine Observing System (IMOS) program, developed by the Australian Ocean Data Network (AODN) to process instruments attached to oceanographic moorings, allowed the velocity data quality control. Empirical orthogonal functions filled the information gaps along the time series. This method does not alter the time series statistics (Beckers and Rixen, 2003). The same method was more recently employed by Rocha et al. (2014) and Simoes-Sousa et al. (2021) off the Brazilian continental margin.

2.1. Model setup

The numerical simulation of the RGR circulation was performed using the Coastal and Regional Ocean COmmunity model (CROCO; Auclair et al., 2019). CROCO is a model constructed over the Regional Ocean Model System - Adaptive Grid Refinement In Fortran (ROMS-AGRIF; Shchepetkin and McWilliams, 2005). The simulation was carried out under the hydrostatic approximation and solved the primitive equations in an Earth-centered rotating environment for potential temperature, salinity, and velocity. CROCO has terrain-following coordinates, and this configuration allowed us to solve the dynamics in the entire model domain using the same amount of vertical levels that adjust to the local topography.

The numerical model domain covers the area between $24^{\circ}W$ and $44^{\circ}W$ in longitude, and $24^{\circ}S$ and $38^{\circ}S$ in latitude, with the RGR in the center of the grid (Fig. 1a). The model's horizontal resolution is $1/50^{\circ}$, approximately 1.8 km. The model has 30 vertical levels refined near the surface and the seafloor.

The model bathymetry was constructed from the General Bathymetric Chart of the Oceans (GEBCO) 2021 (GEBCO Compilation Group, 2021), a global terrain model for ocean and land that provides elevation data on a 15-arc-second interval grid. A Hanning smoothing kernel with 4 bathymetry grid points spacing was used to prevent aliasing in any situation where the bathymetry data has a higher resolution than the model grid and to ensure the bathymetry smoothness at the grid horizontal resolution scale. Terrain-following models like CROCO have computational constraints with respect to the roughness and steepness of the bathymetry (Beckmann and Haidvogel, 1993). According

to Beckmann and Haidvogel (1993), to prevent horizontal pressure gradient errors the model bathymetry requires that the steepness of the topography

$$r = \frac{h_i - h_{i-1}}{h_i + h_{i-1}} \tag{1}$$

does not exceed $r_{max} = 0.2$. Here, h_i is the bathymetry height at the *ith* grid point. In our domain, the maximum value of r is 0.19, and in the RGR domain of interest of this study (Fig. 1b), it reaches 0.15.

We prescribed radiative open boundaries and the initial condition with the Global Ocean Reanalysis and Simulation (GLORYS) 12V1 reanalysis daily outputs from Mercator Ocean (Fernandez and Lellouche, 2018). GLORYS12V1 is a daily eddy-resolving reanalysis that runs on the Nucleus for European Modelling of the Ocean - Ocean General Circulation Model (NEMO-OGCM) using a 1/12°horizontal resolution and 50 vertical levels. The ocean reanalysis is available at E.U. Copernicus Marine Environment Monitoring Service (CMEMS). We also used the European Centre for Medium-Range Weather Forecasts (ECMWF) reanalysis fifth generation (ERA5) atmospheric reanalysis at the surface (Hersbach et al., 2018) with a 6-hour time resolution. At the model boundaries, we additionally prescribed the tidal elevation and barotropic currents from the TOPEX/Poseidon Global Inverse Solution 7 (TPXO7; Egbert and Erofeeva, 2002).

The model ran from January 1 2015 to December 31, 2019. The first three years consisted of model spin-up. All results discussed here span the period between January 2018 and December 2019. In addition to the simulation described above, hereafter Exp-wt, we ran a second experiment with no tidal forcing (Exp-nt). We used the hourly outputs of February 2018 for the tidal analyses and the daily averaged outputs to describe the mean fields for the period between January 2018 and December 2019.

3. Mooring variability

The current meter mooring located on the south slope of the CSR revealed several aspects of the temporal variability within approximately 50 m above the bottom. The flow within the CSR presented an oscillatory pattern caused by tides (Fig. 2b) with velocity peaks that can reach $0.3 \,\mathrm{m \, s^{-1}}$ in magnitude (Fig. 2a). The time series of kinetic energy, KE = $(u^2 + v^2)/2$ (Fig. 2a), shows peaks that reach $0.04 \,\mathrm{m^2 \, s^{-2}}$.

The velocity power spectral density (PSD) reveals important aspects of the oscillatory flows observed at the mooring, identifying the main frequencies responsible for the velocity temporal variability and the associated phenomena. Fig. 2b shows the velocity spectrum, showing that the CSR variability is largely due to the semi-diurnal lunar tidal constituent (M2), with a period of 12.42 h, and by the principal solar semi-diurnal constituent (S2) with a period of 12 h. Although with a variance one order of magnitude smaller than the M2 variance, we also found other relevant constituents: the lunar diurnal constituent (O1) with a period of 25.82 h, and the larger lunar elliptic semi-diurnal constituent (N2) with a period of 12.66 h. The identified tidal constituents are in agreement with those found by Harlamov et al. (2015), with the M2 component being the dominant period.

We evaluate the velocity variance ratio to understand how much of the flow variability is explained by tidal periods and by periods longer and shorter than 36 h, a period approximately 55% longer than the inertial period for the region (23.23 h). First, we estimate the velocity PSD, remove the frequencies smaller than the 95% confidence interval, and reconstruct the velocity time series. Second, we fit and remove the tidal periods from the velocity time series using the *ttide* software package (Pawlowicz et al., 2002). Third, we use a low-passed and high-passed filter of 36 h. Finally, we calculate the velocity variance ratios expressed in percentage values for each depth and calculate the mean value for each ADCP (Fig. 2c). The gap between heights above the bottom occurs due to ADCPs blanking space (Fig. 2c).

High frequencies and tides fit are responsible for approximately 95% of the variance close to the bottom and approximately 70% at the

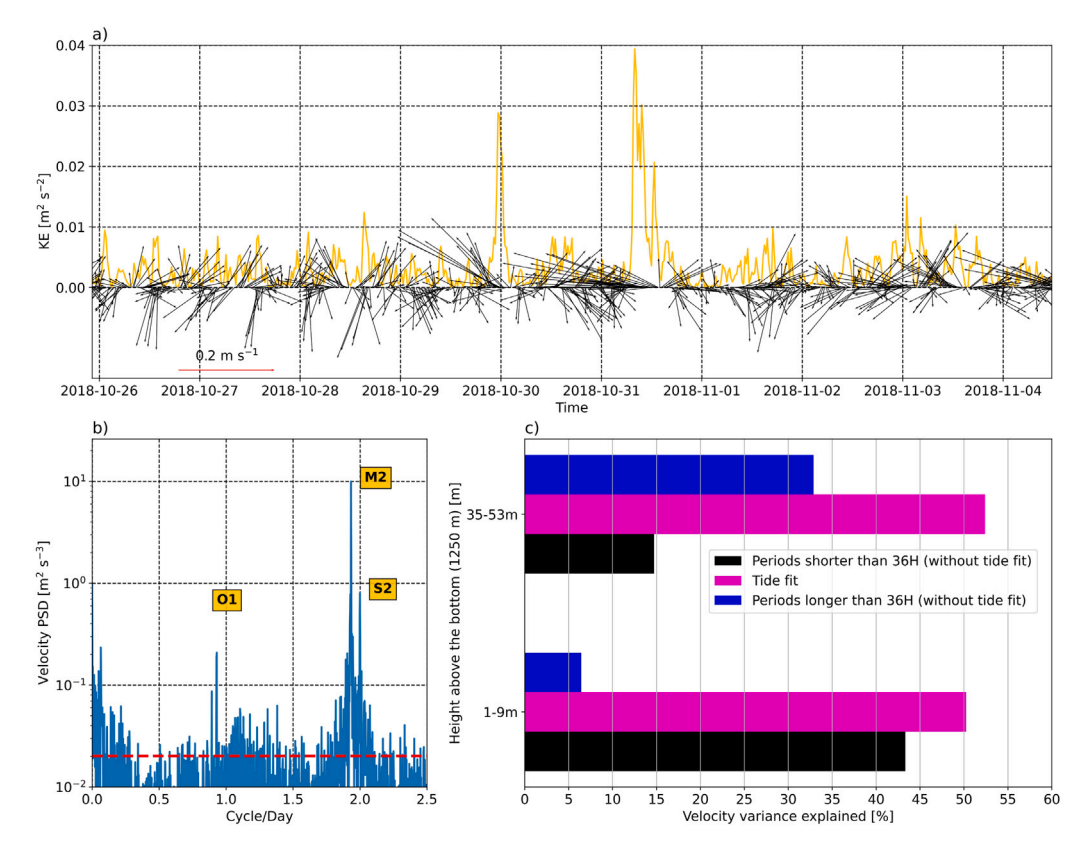


Fig. 2. (a) Velocity (arrows) and KE (yellow line) time series for 10 days, from 10/26/2018 to 11/04/2018 at a depth of 1245 m. (b) Velocity PSD (blue line) and the 95% confidence interval (red dashed line) at 1245 m. (c) Depth-averaged velocity variance ratio for each ADCP comprehending the depth intervals of 1–9 m and 35–53 m above the bottom (1250 m), for the tidal fit periods (magenta bars), for periods shorter than 36 h (without tide fit) (black bars), periods longer than 36 h (without tide fit) (blue bars).

upper-looking ADCP side of the mooring (Fig. 2c). The tidal harmonic fit shows that tides explain almost 50% of the variance in both depth-averaged ADCPs measurements. However, periods shorter than 36 h explain approximately 45% of the variability adjacent to the bottom and 15% above 35 m from the bottom. Regarding the periods longer than 36 h, we observe the increase of the relevance of these frequencies away from the bottom, with the variance explained increasing from 5% to almost 35%

Similar results were found by Lahaye et al. (2019) at the Rift Valley of the North Mid-Atlantic Ridge. They found, using a set of moorings with current meters and a numerical simulation, that the M2 component is predominant. Additionally, Thurnherr et al. (2005) observed 250 m above the bottom of the Mid-Atlantic Ridge Flank the predominance of the M2 and S2 components, with low frequencies representing 40% of the variance of the flow, and the M2 component with near-inertial waves represent 60% of the variance. This result resembles the shallower portions of our mooring, showing a similar variability.

4. Barotropic tides

The mooring data revealed the importance of the tides in the CSR circulation variability, especially the M2 component. However, as we have just one mooring with measurements close to the bottom, we do not have a full understanding of the processes that occur in the RGR, mainly due to the limited vertical and horizontal coverage. We, therefore, resort to the CROCO numerical simulations to investigate the tidal dynamics in the RGR. The model performance was evaluated with the mooring time series and the World Ocean Atlas 2018 (WOA18) dataset (Locarnini et al., 2018; Zweng et al., 2019) as presented in Appendix, where we show that the model temperature and salinity large scale field agrees with those observed in the mooring.

Fig. 3 shows the M2 barotropic amplitude evidencing that the M2 barotropic tides are affected by the local topography. The M2 barotropic amplitude is fitted from the barotropic velocity of the one-month period simulation with an hourly resolution, spanning approximately 54 M2 tidal cycles.

The shallower areas of the RGR display an amplification of M2 barotropic tide, a consequence of mass conservation of uniform barotropic flows. We find a mean amplitude of $0.02\,\mathrm{m\,s^{-1}}$ in areas deeper than 3000 m, and a mean amplitude three times higher at areas shallower than $1200\,\mathrm{m}$, $0.06\,\mathrm{m\,s^{-1}}$. Nevertheless, velocity amplitude peaks can reach $0.1\,\mathrm{m\,s^{-1}}$ at $34.7^{\circ}\mathrm{W-}31.3^{\circ}\mathrm{S}$, close to the mooring location. The M2 barotropic amplitude configuration in RGR is similar to those observed in the Mid-Atlantic Ridge by Zilberman et al. (2009). In both places, the velocity increases due to topographic changes, with the amplitude spanning between $0.02\,\mathrm{m\,s^{-1}}$ and $0.06\,\mathrm{m\,s^{-1}}$.

The mooring measurements show velocity peaks that can reach $0.3\,\text{m}\,\text{s}^{-1}$. However, the barotropic tide's maximum velocities are restricted to the interval of $0.06\text{--}0.1~\text{m}\,\text{s}^{-1}$. The difference between both velocities indicates that barotropic tides alone cannot explain the mooring velocities. In the next section, we will explore the baroclinic tides in the RGR.

5. Internal tides

To comprehend the role of internal tides in the RGR flow variability, we fit the M2 component in a transect at $35.28^{\circ}W$ and at the bottom, shown in Figs. 4a and 4b, respectively. Fig. 4a shows that the M2 velocity amplitude reaches $0.3\,\mathrm{m\,s^{-1}}$, and there is the formation of beams that tracks the areas where the M2 velocity amplitude is maximum. Fig. 4b shows that the areas with the higher amplitudes are located at the RGR summits and in the CSR valley, with a typical amplitude of $0.2\,\mathrm{m\,s^{-1}}$ and peaks reaching $0.3\,\mathrm{m\,s^{-1}}$.

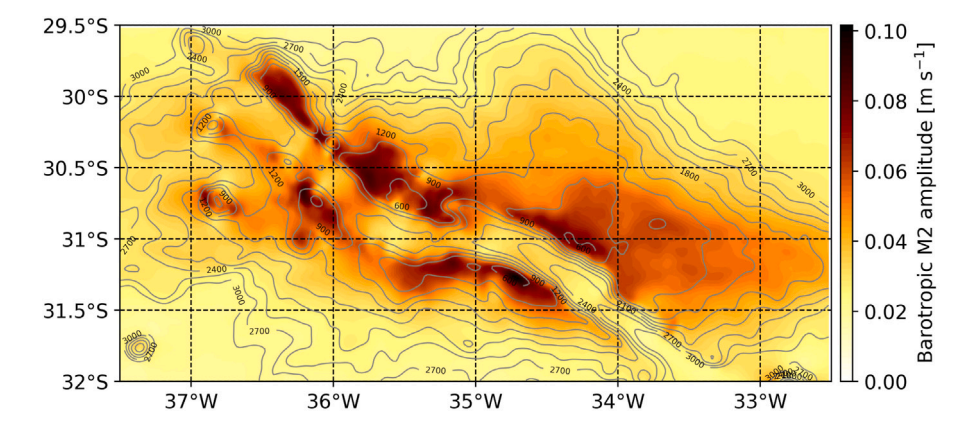


Fig. 3. M2 barotropic amplitude from CROCO simulation in the RGR. The gray lines are isobaths from the smoothed GEBCO bathymetry used in the CROCO simulation.

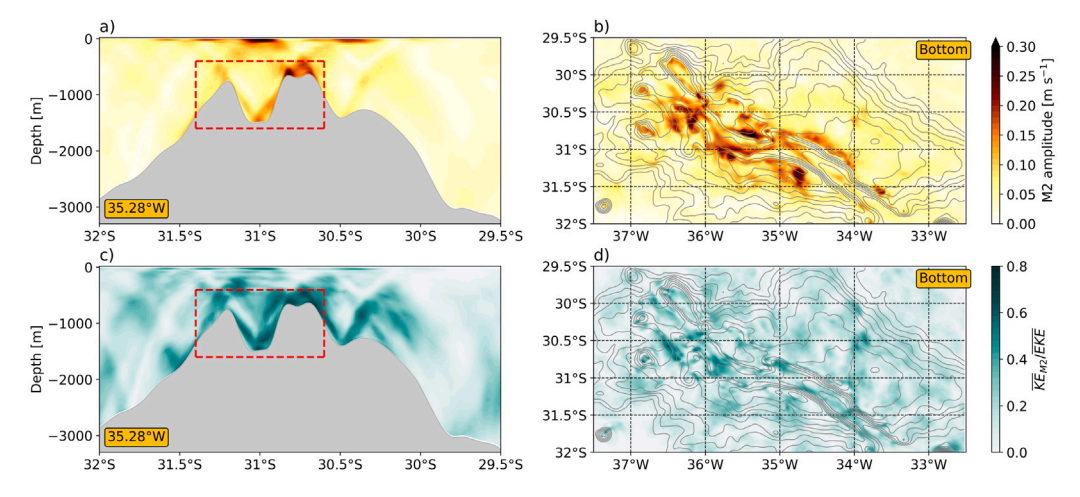


Fig. 4. M2 amplitude from CROCO simulation at (a) a vertical transect at 35.28°W, and (b) at the bottom. The ratio between the mean M2 KE (\overline{KE}_{M2}) and the mean EKE (\overline{EKE}) (c) at a vertical transect in 35.28°W and (d) at the bottom. The red rectangle at (a) and (c) indicates the area where the explained variance was calculated for the 35.28°W transect. The gray lines are isobaths from the smoothed GEBCO bathymetry used in the CROCO simulation.

We quantify the mean M2 kinetic energy (\overline{KE}_{M2}) and the mean eddy kinetic energy (\overline{EKE}) , $EKE = (ur^2 + vr^2)/2$, where ur and vr are deviations from the monthly mean, and we compute the ratio between the \overline{KE}_{M2} and the \overline{EKE} (Figs. 4c and 4d). The ratio reveals that almost 70% of the \overline{EKE} is due to the \overline{KE}_{M2} in certain areas. Also, Fig. 4a reveals tidal beams' paths, which will be explored in the next section.

The coefficient of determination (R^2) between the M2 amplitude and the \overline{EKE} is 89% for the area in the red rectangle present in Figs. 4a and 4c, showing that the M2 amplitude can explain 89% of the eddy flow at the RGR summit. At the bottom, the M2 amplitude and the \overline{EKE} also present a similar pattern, with an explained variance of 86%, showing that the M2 amplitude can explain 86% of the \overline{EKE} of the flow at the bottom.

The velocity amplitude of the barotropic M2 tidal component (Fig. 3) cannot explain alone the total M2 signal. This occurs because the M2 amplitude is typically $0.2\,\mathrm{m\,s^{-1}}$ while the barotropic M2 amplitude is $0.06\,\mathrm{m\,s^{-1}}$. In addition, the bottom M2 amplitude peak in the CSR valley (Fig. 4b) is not present in the barotropic M2 amplitude map (Fig. 3). Lastly, the vertical transect in Fig. 4a suggests intense internal tides due to the vertical changes in the M2 amplitude. Thus, intense internal tides appear to dominate the variability in the RGR.

5.1. Formation of tidal beams

To understand the vertical distribution of the M2 tidal velocity amplitude (Fig. 4a), we explore the possibility of the formation of tidal beams in the region. The dynamical processes that happen along steep

topographies are considerably dependent on the relative steepness of the bottom topography, defined by Garrett and Kunze (2007) as

$$\gamma = \frac{|\nabla H(x, y)|}{\alpha(x, y, -H)},\tag{2}$$

where $|\nabla H(x, y)|$ is the magnitude of the topographic gradient, H is the water column depth, and α is the slope of the internal-tide characteristic path,

$$\alpha(x, y, z) = \pm \sqrt{\frac{\omega^2 - f^2}{N^2(x, y, z) - \omega^2}},$$
(3)

where N(x,y,z) is the time-averaged (2 years) buoyancy frequency, f is the Coriolis parameter, and ω is the tidal frequency for the M2 component.

The relative steepness of the bottom topography determines two different tidal energy conversion regimes. The subcritical regime occurs when $\gamma < 1$ and allows the baroclinic energy to propagate horizontally as low baroclinic modes (Vlasenko et al., 2016). When $\gamma > 1$, we have a supercritical condition that leads to the generation of high baroclinic modes (Stashchuk and Vlasenko, 2017), with the flow concentrated into beams, where the baroclinic tidal energy propagates. The beams are generated at the topography in critical regions, where $\gamma \approx 1$ and the energy radiates in the along-beam direction.

Fig. 5a shows a map of γ , revealing that the CSR slope is supercritical ($\gamma > 1$). Hence, the CSR has an important role in dictating the M2 tidal baroclinic energy propagation, allowing for the formation of tidal beams.

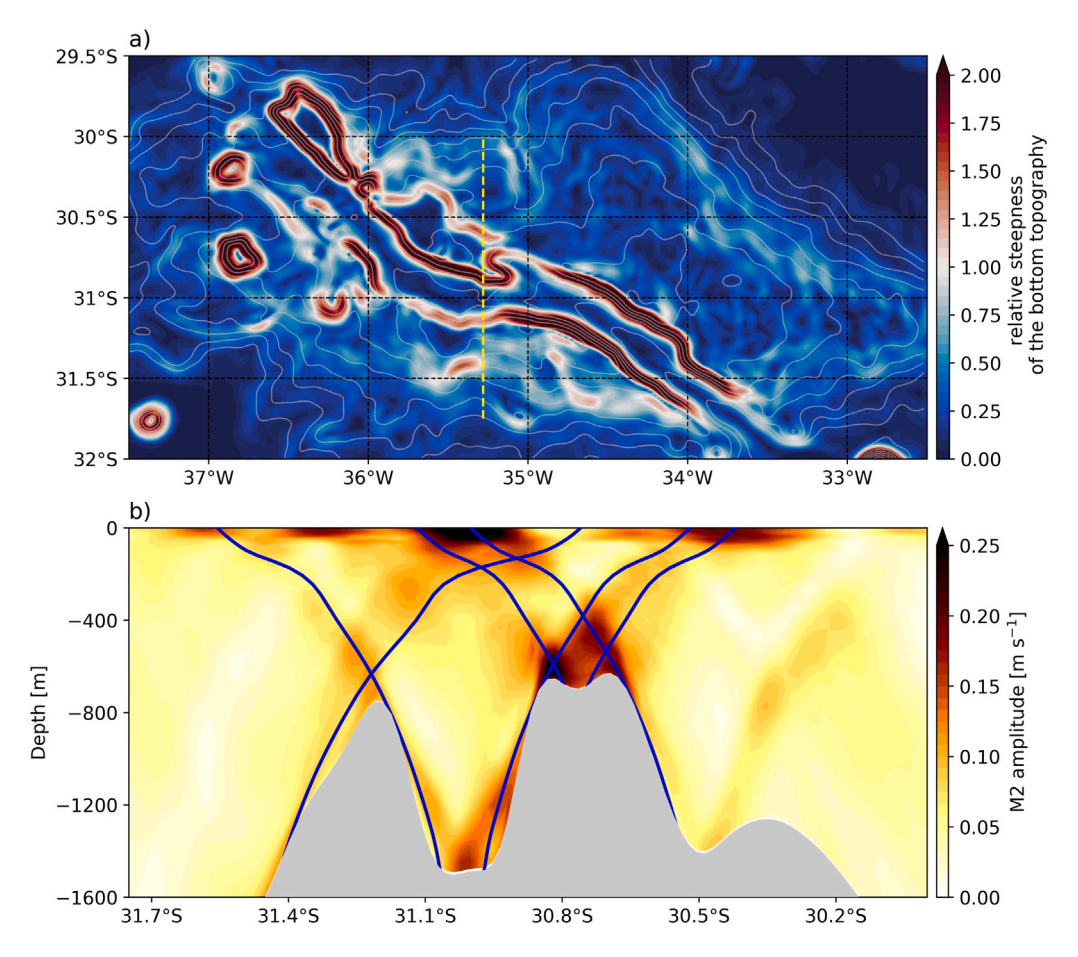


Fig. 5. The formation of tidal beams: (a) map of the relative steepness of the bottom topography. The gray lines are isobaths from the smoothed GEBCO bathymetry used in the CROCO simulation. (b) M2 tidal velocity amplitude with the M2 characteristics paths (blue lines), which originated where $\gamma = 1$. The yellow dashed line at (a) indicates the transect in (b) at 35.28°W.

In Fig. 5b, we observe the formation of six primary tidal beams, two located at the south crest and four at the north crest. The tidal beam pathways have a high correspondence with the M2 amplitude, thus the formation of tidal beams explains the M2 pattern in CSR. One beam of each crest is formed in the CSR slope and propagates to the CSR interior, meeting at the CSR valley (Fig. 5b). At the north crest, we have the formation of three tidal beam interceptions between 400 and 700 m accompanied by a larger M2 amplitude (Fig. 5b).

The formation of tidal beams is relatively common in regions of steep topography, such as the South Brazil Bight (Pereira et al., 2007), the Hawaiian Ridge (Cole et al., 2009), the Mid-Atlantic Ridge (Zilberman et al., 2009), the VTR (Paiva et al., 2018), the Celtic Sea shelf break (Vlasenko et al., 2014), the Malin Sea continental slope (Stashchuk and Vlasenko, 2017) and the Anton Dohrn Seamount (Vlasenko et al., 2018).

5.2. Energetics of the M2 internal tide

In the previous section, we addressed that the CSR slopes are supercritical for the generation of baroclinic tides that propagate along tidal beams (Fig. 5). Now, we seek to understand the M2 tide energetics in the RGR area to depict the conversion sites of barotropic to baroclinic tides and the resulting baroclinic energy fluxes. Thus, following Niwa and Hibiya (2004) and Wang et al. (2016), we estimate the depthintegrated dissipation rate of the baroclinic energy (DIS_{bc}) averaged over one tidal period, assuming that advection of baroclinic energy is negligible:

$$\langle DIS_{bc}\rangle \approx \nabla_h \cdot \vec{F}_{bc} - \langle E_{bt2bc}\rangle, \tag{4}$$

where $\langle \rangle$ denotes the average over one M2 tidal period, $\nabla_h \cdot \vec{F}_{bc}$ is the divergence of the depth-integrated baroclinic energy flux, and E_{bt2bc} is the depth-integrated conversion from barotropic to baroclinic energy:

$$E_{bt2bc} = g \int_{-H}^{\eta} \rho t \, w_{bt} \, dz, \tag{5}$$

$$\nabla_h \cdot \vec{F}_{bc} = \nabla_h \cdot \left\langle \int_{-H}^{\eta} \vec{u}' \, p' \, dz \right\rangle, \tag{6}$$

where H is the water column depth, η is the sea level height and g is the gravity acceleration. We estimate all terms in the energy analysis (4) to (6) by time averaging over 54 tidal cycles. The prime terms denote perturbations in relation to one tidal period for density (ρ) , pressure (p), and horizontal velocities (\vec{u}) . The w_{bi} is the vertical velocity associated with the barotropic flow (Mellor, 2004):

$$w_{bt} = u_{bt} \left(\sigma \frac{\partial D}{\partial x} + \frac{\partial \eta}{\partial x} \right) + v_{bt} \left(\sigma \frac{\partial D}{\partial y} + \frac{\partial \eta}{\partial y} \right) + (\sigma + 1) \frac{\partial \eta}{\partial t}, \tag{7}$$

where $D = \eta + H$, $\sigma = (z - \eta)/D$, and (u_{bt}, v_{bt}) is the barotropic horizontal velocity. The prime terms were calculated following Nash et al. (2005), where

$$\rho'(z,t) = \rho(z,t) - \langle \rho(z) \rangle, \tag{8}$$

$$p'(z,t) = p_{surf}(t) + g \int_{z}^{\eta} \rho'(\hat{z},t) \, d\hat{z}, \tag{9}$$

and p_{surf} is the surface pressure. The depth-averaged baroclinic pressure perturbation must be zero. Hence,

$$\frac{1}{H} \int_{-H}^{\eta} pt(z,t) \, dz = 0. \tag{10}$$

Depth averaging from (9), and using (10), we obtain

$$p_{surf} = -\frac{g}{H} \int_{-H}^{\eta} \left(\int_{z}^{\eta} \rho \prime(\hat{z}, t) \, d\hat{z} \right) \, dz. \tag{11}$$

The perturbation velocity is defined as

$$\vec{u}'(z,t) = \vec{u}(z,t) - \langle \vec{u}(z) \rangle - \vec{u}_{bt}(t), \tag{12}$$

where $\langle \vec{u} \rangle$ is the M2 tidal period mean horizontal velocities. Again, the barotropic velocity is determined by noting that the baroclinic velocity has zero depth average:

$$\frac{1}{H} \int_{-H}^{\eta} \vec{u} t(z, t) \, dz = 0. \tag{13}$$

Therefore, the barotropic horizontal velocity is:

$$\vec{u}_{bl}(t) = \frac{1}{H} \int_{-H}^{\eta} \vec{u}(z,t) - \langle \vec{u}(z) \rangle \, dz. \tag{14}$$

Fig. 6a shows the depth-integrated conversion from barotropic to baroclinic energy, where positive values indicate conversion from barotropic to baroclinic tides. Negative values are attributed to a phase difference greater than 90° between the bottom pressure perturbation and the barotropic vertical velocity (Zilberman et al., 2009; Kerry et al., 2013; Chang et al., 2019). Negative conversions suggest that internal tides generated in different locations interact (Zilberman et al., 2009; Nagai and Hibiya, 2015).

The conversion zone is inhomogeneous on the RGR domain (Fig. 6a), with most of the conversion happening on the CSR slopes, where the mean depth-integrated conversion rate can reach 0.2 W m⁻². M2 conversion rates with a value spanning between 10⁻² W m⁻² and 10⁻¹ W m⁻² were observed by Vic et al. (2019) in the area using a semi-analytical model. Similar conversion rates were found at Monterey Bay (Kang and Fringer, 2012), Southern California Bight (Buijsman et al., 2012), Philippine Sea (Kerry et al., 2013), and West Coast of India (Subeesh et al., 2021). Most of the places of conversion and generation of internal tides coincide with the supercritical and near critical areas of the relative steepness of the bottom topography (Fig. 5a), showing that the internal tides are locally generated. Since our model domain does not cover the area of the VTR (Fig. 1), the Mid-Atlantic Ridge, and the Santos Basin, we are not able to evaluate remote internal tides that could interact with those formed in the RGR. Also, it is important to outline that tidal beams formed in the VTR were observed propagating at the surface until 30°S-36.5°W (Paiva et al., 2018).

Moreover, the depth-integrated baroclinic energy flux (Fig. 6b) shows that after being converted from barotropic energy at the summits, the baroclinic energy develops streams diverging and propagating away from the RGR summits, corroborating the existence of the tidal beams. The streams reach 1.2 kW m⁻¹ in the center of the RGR and about 0.6 kW m⁻¹ from those emanating from the western summit at 30°S-36.5°W. Stronger fluxes in the western portion of the RGR were also observed by Paiva et al. (2018) from altimetry estimations of the mode-1 M2 internal tides, their estimations show that in the entire RGR domain the fluxes are higher than $0.5\,\mathrm{kW}\,\mathrm{m}^{-1}$ and can reach up to 1-2 kW m⁻¹ (value inferred from our visual inspection from Figure 7 from Paiva et al. (2018)). Estimates of mode-1 M2 internal tide flux from Toffoli et al. (2023) using other satellite data do not show any energy flux increase in the RGR domain or fluxes higher than $0.5 \,\mathrm{kW}\,\mathrm{m}^{-1}$. Additionally, the divergence of the depth-integrated baroclinic energy flux (Fig. 6c) presents a similar pattern and magnitude to the depthintegrated conversion rate, an indication that most of the energy that is converted is radiated. Most divergence happens in the CSR slopes and convergence in the CSR interior. This creates a banded pattern of divergence, suggesting that the CSR slopes are the internal-tide energy source region, while the CSR interior is a sink region.

Finally, the depth-integrated dissipation rate of the baroclinic energy present peaks at the CSR slopes (negative values, Fig. 6d). At the slopes, where the conversion rate is greater than $6.25\,\mathrm{mW\,m^{-2}}$

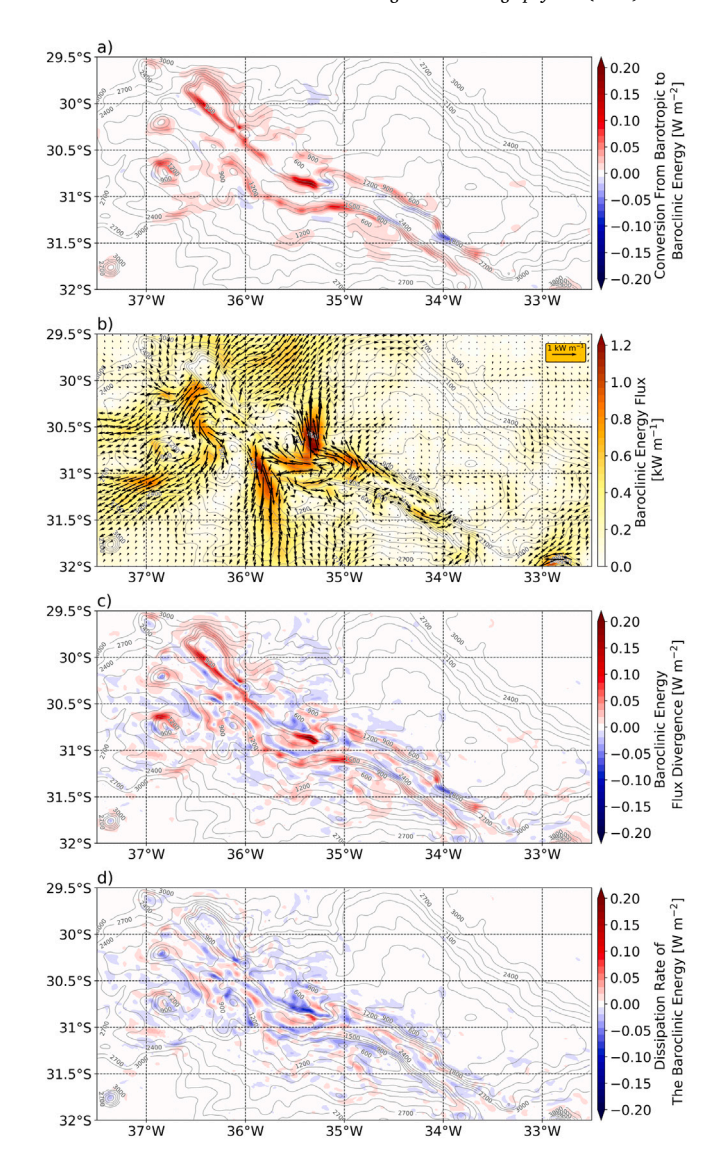


Fig. 6. Energetics of the M2 internal tides: (a) depth-integrated conversion from M2 barotropic tide energy to M2 baroclinic tide energy, (b) depth-integrated M2 baroclinic energy flux, (c) depth-integrated M2 baroclinic energy flux divergence, and (d) depth-integrated dissipation rate of the M2 baroclinic energy. The gray lines are isobaths from the smoothed GEBCO bathymetry used in the CROCO simulation.

(red areas, Fig. 6a), the area-integrated baroclinic energy conversion accounts for a total of 0.36 GW, whereas 84.8% radiates, while 15.2% is locally dissipated. However, the area-integrated baroclinic energy conversion for all the domain is 0.37 GW, where 52.9% of the converted baroclinic energy is dissipated, and 47.1% is radiated away. Our estimated fraction of dissipation is in agreement with those found by Vic et al. (2019). The authors compute the ratio of the local energy dissipation with the total energy conversion globally, the RGR area presents a ratio spanning between 0.4-0.7. From those 52.9% that is dissipated of the area-integrated baroclinic energy conversion for all domain, 38.2% is dissipated during the propagation of the M2 internal tides, and 14.7% is dissipated directly in the M2 internal tides generation sites. Furthermore, it is fair to mention the caveat of our dissipation estimation is a residual since we do not consider secondorder non-linear terms. Areas with positive values of dissipation can be related to numerical noise at the model (Zilberman et al., 2009) and to second-order non-linear terms not considered at (4) (Buijsman et al., 2012).

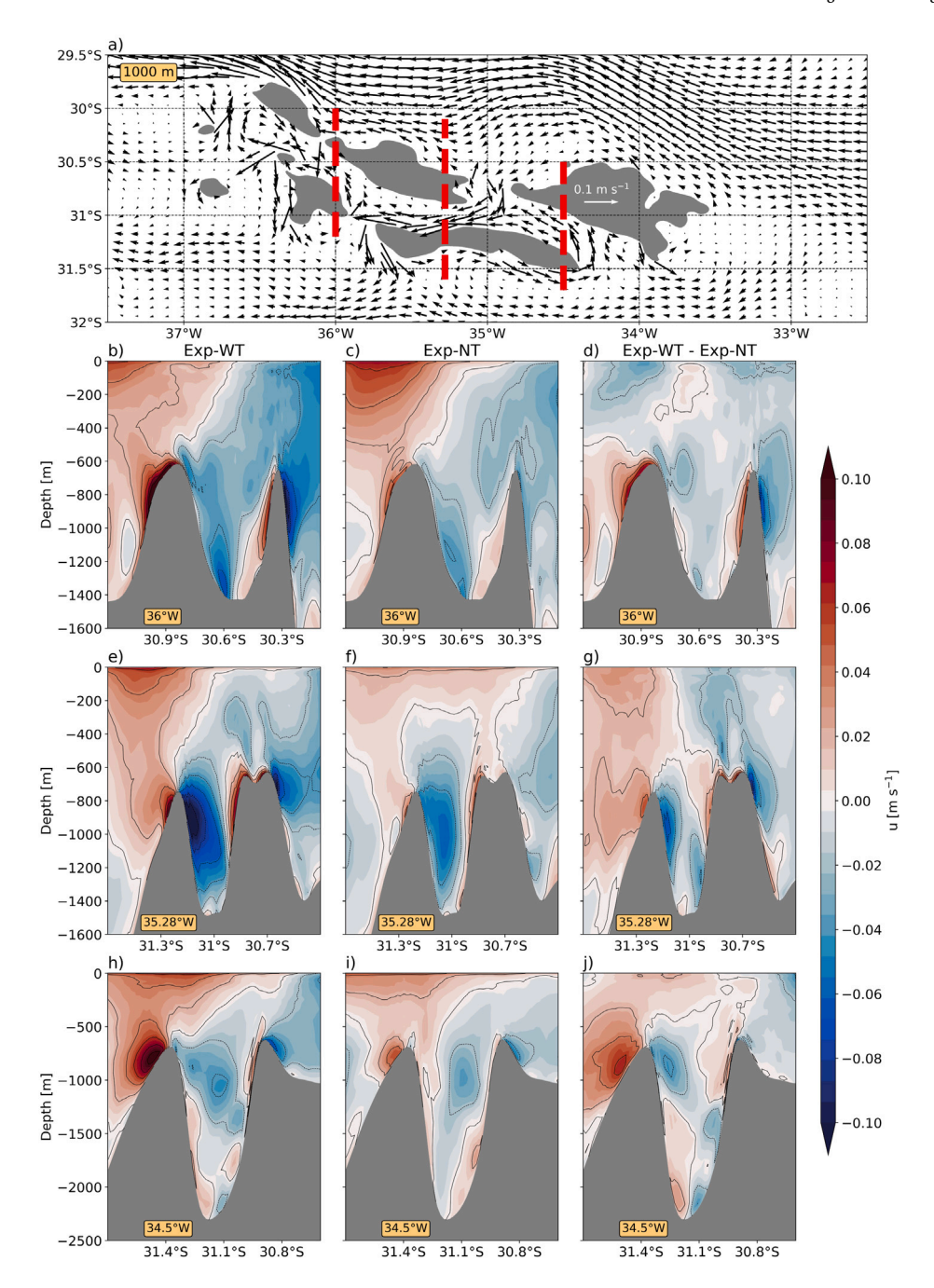


Fig. 7. (a) Exp-wt 2-year velocity average horizontal field at 1000 m. 2-year zonal velocity average transects at 36°W, 35.28°W, and 34.5°W, for Exp-wt at (b), (e) and (h), respectively, and for Exp-nt at (c), (f) and (i). The difference between both experiments (Exp-wt - Exp-nt), for each one of the transects at (d) 36°W (g) 35.28°W and (j) 34.5°W.

6. Anticyclonic circulation

The Exp-wt 2-year mean velocity field at 1000 m evidences the bifurcation of the 30°S sSEC branch, and the presence of anticyclonic circulations around the RGR summits (Fig. 7a). The vertical transects of the Exp-wt located at 36°W (Fig. 7b), 35.28°W (Fig. 7e), and 34.5°W (Fig. 7h) reveal that the depth range of the anticyclonic circulation varies spatially, being confined mainly between 500–1500 m, with the velocity lobes being able to reach $0.1\,\mathrm{m\,s^{-1}}$. Due to the anticyclonic circulations in the southern side of the CSR being larger, their westward velocity lobe occupies most of the area inside the CSR (Figs. 7b, 7e and 7h).

In the RGR, there is evidence that suggests the formation of the anticyclonic circulations by the two processes: an impinging mean flow and tidal rectification. First, there is the presence of the sSEC impinging

on the RGR topography, and second, the M2 tidal component is the principal source of super-inertial variability. Evaluating the relative importance of each tidal component to the generation of tidally rectified mean flows is not easy due to the complexity of the physical environment (González-Pola et al., 2012), however, Wright and Loder (1985) and Freeland (1994) provided an analytical expression to estimate the maximum mean flow that can be generated by tidal rectification for a specific tidal component:

$$\overline{u} \approx \frac{3fV_0^2}{2\omega^2 h} \frac{dh}{dr},\tag{15}$$

where f is the Coriolis parameter, V_0 is the amplitude of the tidal current, h is the local depth, ω is the angular frequency of the tidal component, and dh/dr is the slope gradient. Considering V_0 equal to $0.3\,\mathrm{m\,s^{-1}}$ for the M2 tidal component (Figs. 4a and 4b), dh/dr equal to

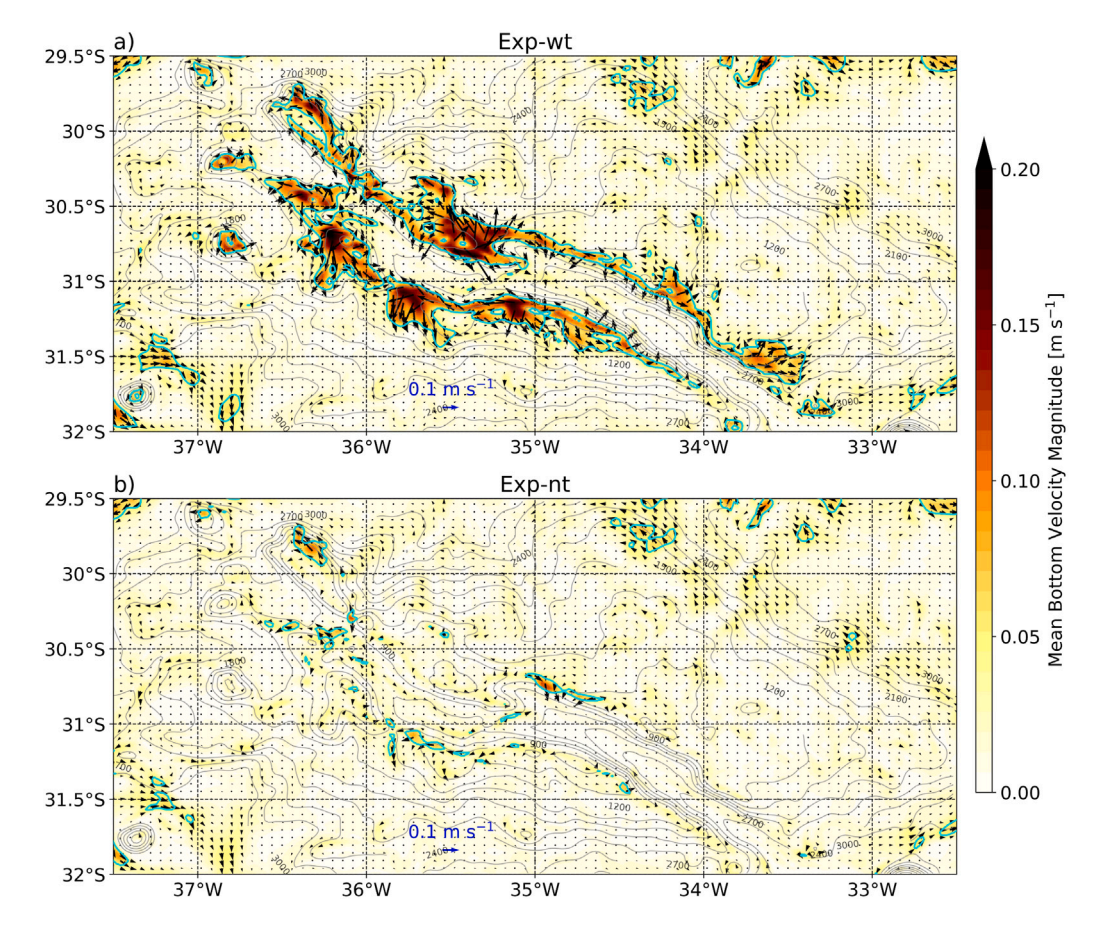


Fig. 8. A 2-year horizontal velocity average field at the bottom (a) Exp-wt and (b) Exp-nt. The gray lines are isobaths from the smoothed GEBCO bathymetry used in the CROCO simulation. The cyan lines are the $0.05\,\mathrm{m\,s^{-1}}$ contour.

0.21 (maximum value inside the CSR), and taking h as the minimum depth of 500 m, the estimated maximum rectified flow for the M2 component is $0.2\,\mathrm{m\,s^{-1}}$. This result shows that tidal rectification can contribute to a significant proportion of the mean flow.

To better understand which mechanisms are responsible for the formation of the anticyclonic circulation, we compare the realistic numerical experiment (Exp-wt) with the numerical experiment without tidal forcing (Exp-nt) to evaluate how the presence of tides modifies the mean flow.

Vertical transects for the Exp-nt (Figs. 7c, 7f and 7i) reveal the decrease of the anticyclonic circulation in about 50% when compared with the Exp-wt (Figs. 7b, 7e and 7h), and in some places, it almost vanishes when compared with the respective transects of Exp-wt, as observed when comparing the northern summit in Figs. 7h and 7i. To estimate the anticyclonic circulation generated only by tidal effects, we compute the difference between the Exp-wt and the Exp-nt (Figs. 7d, 7g and 7j). We observe that tides are responsible for creating an anticyclonic circulation with at least the same magnitude of the Exp-nt. Figs. 7d, 7g and 7j present most cores of the anticyclonic circulation stronger $0.02\,\mathrm{m\,s^{-1}}$ when compared to Exp-nt.

The anticyclonic circulation pattern can also be depicted adjacent to the bottom. Fig. 8a shows the anticyclonic circulation at the RGR summits (Exp-wt) with mean bottom velocity reaching $0.2\,\mathrm{m\,s^{-1}}$. On the other hand, the mean circulation in the CSR valley presents nearly zero velocities in almost the entire domain, with a few sparse patches of velocities higher than $0.05\,\mathrm{m\,s^{-1}}$. The velocity increases close to the CSR west opening around 36°W. Examining the mean bottom velocity from Exp-nt (Fig. 8b), we observe that the anticyclonic pattern virtually disappears and the velocity field became much weaker in all RGR summits. Therefore, despite tides and the impinging mean flow supplying the formation of the anticyclonic circulation almost

equally, tides are responsible almost entirely for the flow intensification adjacent to the bottom in the RGR summits. This result is corroborated by the maximum rectified flow of $0.2\,\mathrm{m\,s^{-1}}$, obtained by Eq. (15).

Depending on the regional setup, either the mean flow impingement or tidal rectification can be dominant. Many local physical variables are relevant to evaluate the relative importance of these processes to the anticyclonic circulation development, such as stratification, Coriolis parameter, topography gradient and height, the amplitude of the tidal forcing, and periods of steady impinging flows (Guo et al., 2020; González-Pola et al., 2012). For example, the Caiwei Guyot in Northwest Pacific was studied using 3 years of mooring data, and Guo et al. (2020) showed that the impinging mean flow is responsible for the anticyclonic formation with the interaction between the M2 tidal component and the topography playing a secondary role. At Le Danois Bank on the continental shelf of the central Cantabrian Sea (Bay of Biscay), González-Pola et al. (2012) show using a set of in situ observations that the M2 tidal rectification plays a major role in dictating the anticyclonic circulation with the impinging mean flow as a second factor.

The comparison between both experiments reveals that tides and the impinging mean flow are almost equally relevant to the formation of anticyclonic circulations. However, tidal rectification is the dominant dynamic process at play in the development of the bottom intensification of the anticyclonic circulations. The impinging mean flow plays a secondary role, associated with a much weaker bottom anticyclonic recirculation.

7. Summary and conclusions

In the present study, we investigated the RGR dynamics, addressing the structure of the mean circulation and its variability. Tides are the principal source of variability in the region and are responsible for intensifying the mean field.

The M2 tidal component is by far the main source of variability in the region, accounting for approximately 90% of flow variability. To understand the role of the M2 tidal energy, we investigated the generation, propagation, and dissipation of the M2 baroclinic energy showing that the CSR slope is supercritical for the M2 internal tides, where most of the conversion from the barotropic to baroclinic energy happens. This conversion is largely balanced by energy flux divergence, indicating that the baroclinic energy radiates away from the RGR summits in the form of tidal beams.

The RGR is a hotspot for baroclinic energy conversion like the Mid-Atlantic Ridge and other submerged canyons (Zilberman et al., 2009; Kang and Fringer, 2012). Despite the VTR being the largest hotspot of internal tides in the Southwestern Atlantic, the RGR slopes, mainly those in the CSR, must be well represented in numerical models for accurate simulation of internal tide generation with consistent energy budgets.

In regards to the mean field, we report the formation of an anticyclonic circulation around the RGR summits. In the literature, there exist two major processes that drive this kind of feature: the presence of an impinging mean flow and tidal rectification. In RGR, both mechanisms are relevant: an sSEC-impinging mean flow and the presence of intense internal tides dominated by the M2 component. Our analyses reveal that both processes are almost equally relevant in the RGR, both generating anticyclonic circulations with the same magnitude, however, tidal rectification allows the development of a bottom intensified anticyclonic circulation that can reach $0.2\,\mathrm{m\,s^{-1}}$.

We also show that the areas with higher M2 tidal amplitude are located in the RGR summits and at the CSR valley, where the amplitude reaches $0.3\,\mathrm{m\,s^{-1}}$. This pattern can be at least partially explained by the existence of tidal beams that develop in areas with steep topography, especially on the CSR slope.

The areas with high M2 tidal amplitude and the mean flow presented in this study could explain the distribution of Fe-Mn crusts, as well as the carbonate plates (Figure 61 in Lisniowski, 2020). The Fe-Mn crusts appear to be mostly located in areas where the tidal amplitude surpasses $0.2\,\mathrm{m\,s^{-1}}$ and the mean flow is greater than $0.1\,\mathrm{m\,s^{-1}}$, which might prevent deposition, thus allowing the crusts to outcrop. Carbonate plates, on the other hand, appear to be mostly located in areas with lower tidal velocities. Therefore, future research regarding the interaction between the tidal and mean flow with the local topography is necessary for understanding the distribution of Fe-Mn crusts and carbonate areas.

CRediT authorship contribution statement

Pedro W.M. Souza-Neto: Writing – review & editing, Writing – original draft, Visualization, Validation, Methodology, Investigation, Formal analysis, Data curation, Conceptualization. Ilson C.A. da Silveira: Writing – review & editing, Writing – original draft, Supervision, Resources, Methodology, Investigation, Conceptualization. Cesar B. Rocha: Writing – review & editing, Writing – original draft, Supervision, Investigation, Conceptualization. Cauê Z. Lazaneo: Writing – original draft, Investigation, Conceptualization. Paulo H.R. Calil: Writing – original draft, Methodology, Conceptualization.

Declaration of competing interest

The authors declare the following financial interests/personal relationships which may be considered as potential competing interests: Pedro Walfir Souza-Neto reports financial support was provided by FAPESP. Pedro Walfir Souza-Neto reports financial support was provided by Coordination of Higher Education Personnel Improvement.

Data availability

Data will be made available on request.

Acknowledgments

The scientific cruise to RGR was funded by Fundação de Amparo à Pesquisa do Estado de São Paulo (FAPESP), Brazil by the research grant 14/50820-7 under the thematic project "Marine ferromanganese deposits: a major resource of E-tech elements". This work is developed within the projects: Universidade de São Paulo through the Edital de Apoio a Projetos Integrados de Pesquisa em Áreas Estratégicas, PIPAE (2021.1.10424.1.9) and "Estudo Multidisciplinar de Novos Minerais Estratégicos e Avaliação de Risco da Mineração na Elevação de Rio Grande (Atlântico Sul) - e-MERG", Ref. Finep n° 0013/21. The authors acknowledge the crew and scientists in the R/V Alpha Crucis during the Marine-Etech Experiment. PWSN acknowledges the financial support from CAPES (Processes Number: 88887.474629/2020-00 and 88887.921522/2023-00) and FAPESP (Process Number: 2020/04315-0). ICAS acknowledges support from CNPq (Grant 309656/2021-4), HidroSan I Project (CNPq 405593/2021-0), HidroSan II Project (FAPESP 2021/13124-6), and REMARSUL Project (CAPES 88882.158 621/2014-01). CBR acknowledges support from the National Science Foundation, United States (award 2146729).

Appendix. Model performance

To evaluate the model performance we compared the model 2-year mean field with the World Ocean Atlas 2018 (WOA18, Locarnini et al., 2018 and Zweng et al., 2019). Also, we compared the mooring velocity time series with the model velocity time series in the closest grid point to the mooring location.

To test the skill of the model mean hydrographic field, we compare it with an independent database, the WOA 2018 climatological mean field from 1955 to 2017 with a horizontal resolution of 1/4°. We use the temperature and salinity data to conduct the skill test. We construct surface-bottom transects in the meridional direction (Fig. A.9) using the temperature and salinity data. The salinity transect located at 34.5°W between 36°S and 26°S for the CROCO model output and the WOA data (Figs. A.9a and A.9b, respectively) shows a good similarity with a root mean square error of 0.11. In these transects, the isohalines are located at the same depth range at the surface and the bottom regards the data and bathymetry differences. The major difference appears south of RGR between 32°S and 34°S around 2500 m, where the WOA transect presents a saltier tongue than the model output, with values surpassing 34.9. The temperature transect located at 34.5°W between 36°S and 26°S for the CROCO model output and the WOA data (Figs. A.9c and A.9d, respectively) also presents good similarity with a root mean square error of 0.33. In these transects, the isotherms have a similar vertical distribution, despite the differences in the data sources and bathymetric resolution.

To test the skill of the CROCO model output variability, we compare the velocity time series of the closest grid point cell to the mooring location with the mooring time series. Since the predominant phenomena observed in the mooring data are related to the M2 tides, we select one month with a one-hour resolution to compare both time series. The period selected corresponds to February 2018. The period of only one month was chosen due to a computational limitation to store high temporal resolution outputs.

We plot both time series and compare their mean velocity components and the velocity variance (Fig. A.10). Fig. A.10 shows a similar variability between both time series, where the velocity can reach $0.2\,\mathrm{m\,s^{-1}}$ and tides dominate. The last characteristic leads to an almost zero mean velocity in both components on the mooring and in the CROCO output. Both velocity series present a similar variance. The biggest difference between both time series is in the meridional velocity

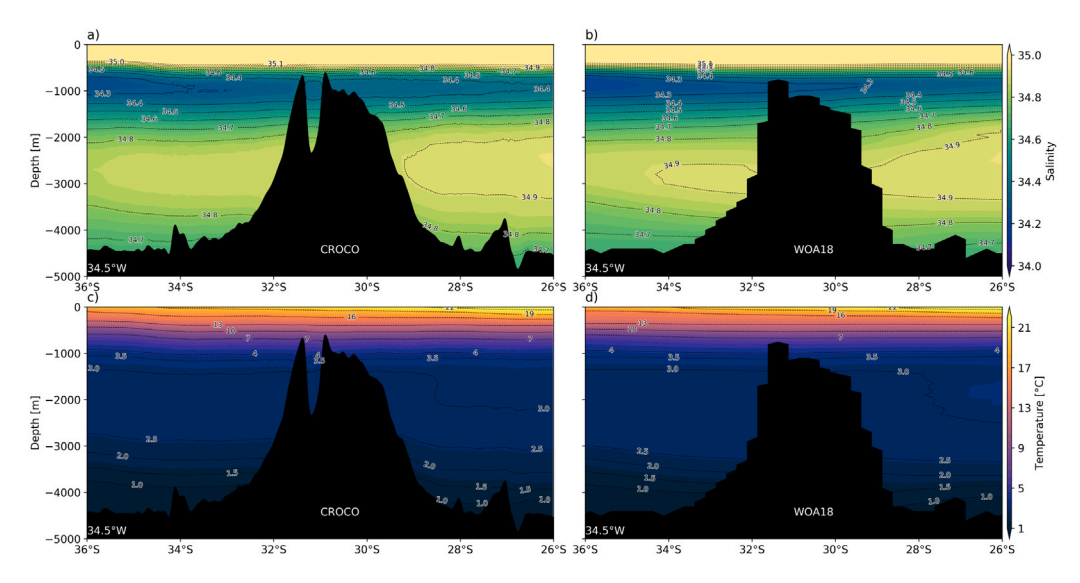


Fig. A.9. Mean salinity transects at $34.5^{\circ}W$ between $26^{\circ}S$ and $36^{\circ}S$ for (a) the CROCO model output and (b) the WOA18 dataset. Mean temperature transects at $34.5^{\circ}W$ between $26^{\circ}S$ and $36^{\circ}S$ for (c) the CROCO model output and (d) the WOA18 dataset.

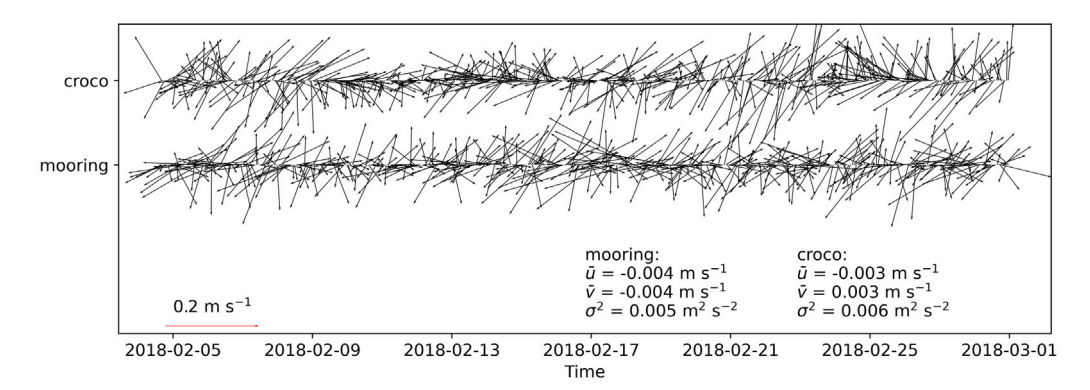


Fig. A.10. Mooring and CROCO model output velocity time series for February 2018 with one-hour resolution. The time series statistic are the mean zonal velocity (\bar{u}) , mean meridional velocity (\bar{v}) and the variance (σ^2) .

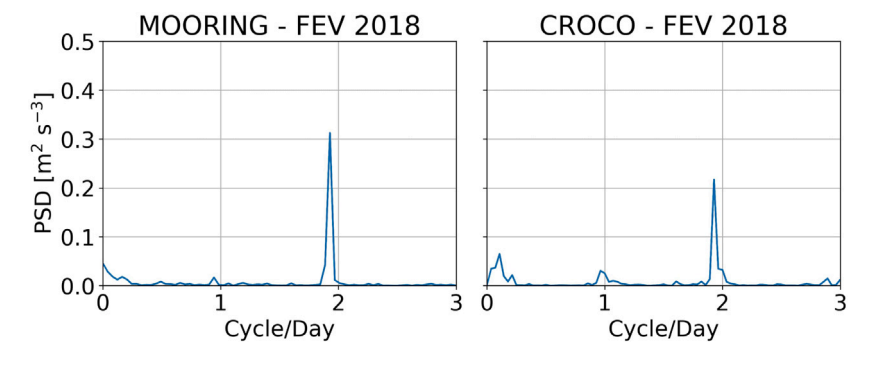


Fig. A.11. Velocity PSD for February 2018 with a one-hour resolution for (a) Mooring velocity time series and (b) CROCO model output velocity time series.

direction, where the mooring presents a southward mean velocity while the CROCO output presents a northward mean velocity.

To test the skill of the model in reproducing the M2 tide component observed in the mooring data (Fig. 2b) as being the principal source of variability in the CROCO model output, we plot the PSD for the CROCO and mooring velocity time series (Fig. A.11) with one-hour resolution. Fig. A.11 shows that the CROCO velocity time series PSD has the same signature observed in the mooring data PSD. The M2 component dominates, followed by the O1 component, and the S2 component is distinguishable in the CROCO PSD (Fig. A.11b) however we depicted

the signal in the full-time series mooring PSD (Fig. 2b). These results indicate that the model variability agrees with the mooring variability.

The differences observed here can be easily caused by the fact that the mooring is located close to the CSR slope (Fig. 1), a place with several trenches as observed by Lisniowski et al. (2017). Also, the model bathymetry has a resolution of approximately 2 km with additional smoothing to avoid pressure gradient errors (see Section 2.1). Because of that, probably the local circulation found where the mooring was deployed cannot be represented perfectly. Furthermore, the hydrographic field and the variability of the model are in agreement with the WOA18 and the Marine E-Tech Mooring, respectively.

References

- Auclair, F., Benshila, R., Bordois, L., Boutet, M., Brémond, M., Caillaud, M., Cambon, G., Capet, X., Debreu, L., Ducousso, N., Dufois, F., Dumas, F., Ethé, C., Gula, J., Hourdin, C., Illig, S., Jullien, S., Corre, M.L., Gac, S.L., Gentil, S.L., Lemarié, F., Marchesiello, P., Mazoyer, C., Morvan, G., Nguyen, C., Penven, P., Person, R., Pianezze, J., Pous, S., Renault, L., Roblou, L., Sepulveda, A., Theetten, S., 2019. Coastal and regional ocean community model. http://dx.doi.org/10.5281/zenodo. 7415133.
- Bashmachnikov, I., Loureiro, C., Martins, A., 2013. Topographically induced circulation patterns and mixing over Condor seamount. Deep Sea Res. Part II: Top. Stud. Oceanogr. 98, 38–51. http://dx.doi.org/10.1016/j.dsr2.2013.09.014.
- Beckers, J.M., Rixen, M., 2003. EOF calculations and data filling from incomplete oceanographic datasets. J. Atmos. Ocean. Technol. 20 (12), 1839–1856. http://dx.doi.org/10.1175/1520-0426(2003)020<1839:ECADFF>2.0.CO;2.
- Beckmann, A., Haidvogel, D.B., 1993. Numerical simulation of flow around a tall isolated seamount. Part I: Problem formulation and model accuracy. J. Phys. Oceanogr. 23 (8), 1736–1753. http://dx.doi.org/10.1175/1520-0485(1993) 023<1736:NSOFAA>2.0.CO;2.
- Benites, M., González, J., Hein, J., Marino, E., Reyes, J., Millo, C., Jovane, L., 2023. Controls on thechemicalcomposition of ferromanganese crusts from deep-water to the summit of the Rio Grande rise, South Atlantic Ocean. Mar. Geol. 107094. http://dx.doi.org/10.1016/j.margeo.2023.107094.
- Benites, M., Hein, J.R., Mizell, K., Blackburn, T., Jovane, L., 2020. Genesis and evolution of ferromanganese crusts from the summit of Rio Grande Rise, Southwest Atlantic Ocean. Minerals 10 (4), 349. http://dx.doi.org/10.3390/min10040349.
- Benites, M., Hein, J.R., Mizell, K., Jovane, L., 2021. Miocene phosphatization of rocks from the summit of Rio Grande Rise, Southwest Atlantic Ocean. Paleoceanography and Paleoclimatology 36 (9), e2020PA004197. http://dx.doi.org/10.1029/ 2020PA004197.
- Buijsman, M., Uchiyama, Y., McWilliams, J., Hill-Lindsay, C., 2012. Modeling semidiurnal internal tide variability in the Southern California Bight. J. Phys. Oceanogr. 42 (1), 62–77. http://dx.doi.org/10.1175/2011JPO4597.1.
- Carter, G., 2010. Barotropic and baroclinic M2 tides in the Monterey Bay region. J. Phys. Oceanogr. 40 (8), 1766–1783. http://dx.doi.org/10.1175/2010JPO4274.1.
- Cavalcanti, J.A.D., Santos, R.V., Lacasse, C.M., Rojas, J.N.L., Nobrega, M., 2015. Potential mineral resources of phosphates and trace elements on the Rio Grande Rise, South Atlantic Ocean. Nearshore underwater mining: Critical commodities for the future UMC.
- Chang, H., Xu, Z., Yin, B., Hou, Y., Liu, Y., Li, D., Wang, Y., Cao, S., Liu, A.K., 2019. Generation and propagation of M2 internal tides modulated by the Kuroshio northeast of Taiwan. J. Geophys. Res.: Oceans 124 (4), 2728–2749. http://dx.doi.org/10.1029/2018JC014228.
- Chapman, D.C., Haidvogel, D.B., 1992. Formation of Taylor caps over a tall isolated seamount in a stratified ocean. Geophys. Astrophys. Fluid Dyn. 64 (1–4), 31–65. http://dx.doi.org/10.1080/03091929208228084.
- Chen, C., Beardsley, R.C., 1995. A numerical study of stratified tidal rectification over finite-amplitude banks. Part I: Symmetric banks. J. Phys. Oceanogr. 25 (9), 2090–2110. http://dx.doi.org/10.1175/1520-0485(1995)025<2090:ANSOST> 2.0.CO:2.
- Cole, S., Rudnick, D., Hodges, B., Martin, J., 2009. Observations of tidal internal wave beams at Kauai Channel, Hawaii. J. Phys. Oceanogr. 39 (2), 421–436. http://dx.doi.org/10.1175/2008JPO3937.1.
- Egbert, G.D., Erofeeva, S.Y., 2002. Efficient inverse modeling of barotropic ocean tides. J. Atmos. Ocean. Technol. 19 (2), 183–204. http://dx.doi.org/10.1175/1520-0426(2002)019<0183:EIMOBO>2.0.CO;2.
- Fernandez, E., Lellouche, J., 2018. Product user manual for the global ocean physical reanalysis product GLOBAL_REANALYSIS_PHY_001_030. EU Copernicus Mar. Serv. http://dx.doi.org/10.48670/moi-00021.
- Freeland, H., 1994. Ocean circulation at and near Cobb Seamount. Deep Sea Res. Part
 I: Oceanogr. Res. Pap. 41 (11–12), 1715–1732. http://dx.doi.org/10.1016/0967-0637(94)90069-8
- Garrett, C., Kunze, E., 2007. Internal tide generation in the deep ocean. Annu. Rev. Fluid Mech. 39, 57–87. http://dx.doi.org/10.1146/annurev.fluid.39.050905. 110227.
- GEBCO Compilation Group, 2021. The GEBCO_2021 Grid-a continuous terrain model of the global oceans and land. http://dx.doi.org/10.5285/c6612cbe-50b3-0cff-e053-6c86abc09f8f.
- González-Pola, C., del Río, G.D., Ruiz-Villarreal, M., Sánchez, R.F., Mohn, C., 2012. Circulation patterns at Le Danois Bank, an elongated shelf-adjacent seamount in the Bay of Biscay. Deep Sea Res. Part I: Oceanogr. Res. Pap. 60, 7–21. http://dx.doi.org/10.1016/j.dsr.2011.10.001.
- Guo, B., Wang, W., Shu, Y., He, G., Zhang, D., Deng, X., Liang, Q., Yang, Y., Xie, Q., Wang, H., et al., 2020. Observed deep anticyclonic cap over Caiwei Guyot. J. Geophys. Res.: Oceans 125 (10), e2020JC016254. http://dx.doi.org/10.1029/ 2020JC016254.
- Haidvogel, D.B., Beckmann, A., Chapman, D.C., Lin, R.Q., 1993. Numerical simulation of flow around a tall isolated seamount. Part II: Resonant generation of trapped waves. J. Phys. Oceanogr. 23 (11), 2373–2391. http://dx.doi.org/10.1175/1520-0485(1993)023<2373:NSOFAA>2.0.CO;2.

- Harlamov, V., Lisniowski, M., Frazão, E., Pessoa, J., Aguiar, R., Lopes, V., Nobrega, M., Lisboa, M., Simões, H., Cavalacanti, J., et al., 2015. Preliminary results on middepth circulation features on Rio Grande Rise. In: 2015 IEEE/OES Acoustics in Underwater Geosciences Symposium (RIO Acoustics). IEEE, pp. 1–8. http://dx.doi.org/10.1109/RIOAcoustics.2015.7473647.
- Hein, J.R., Mizell, K., Koschinsky, A., Conrad, T.A., 2013. Deep-ocean mineral deposits as a source of critical metals for high-and green-technology applications: Comparison with land-based resources. Ore Geol. Rev. 51, 1–14. http://dx.doi.org/10.1016/j.oregeorev.2012.12.001.
- Hersbach, H., Bell, B., Berrisford, P., Biavati, G., Horányi, A., Muñoz Sabater, J., Nicolas, J., Peubey, C., Radu, R., Rozum, I., et al., 2018. ERA5 hourly data on pressure levels from 1979 to present, Copernicus Climate Change Service (C3S) Climate Data Store (CDS). http://dx.doi.org/10.24381/cds.bd0915c6.
- Jovane, L., Hein, J.R., Yeo, I.A., Benites, M., Bergo, N.M., Correa, P.V.F., Couto, D.d., Guimarães, A.D.F., Howarth, S.A., Miguel, H., et al., 2019. Multidisciplinary scientific cruise to the Rio Grande Rise. Front. Mar. Sci. 6, 252. http://dx.doi. org/10.3389/fmars.2019.00252.
- Kang, D., Fringer, O., 2012. Energetics of barotropic and baroclinic tides in the Monterey Bay area. J. Phys. Oceanogr. 42 (2), 272–290. http://dx.doi.org/10.1175/ JPO-D-11-039.1.
- Kerry, C.G., Powell, B.S., Carter, G.S., 2013. Effects of remote generation sites on model estimates of M2 internal tides in the Philippine Sea. J. Phys. Oceanogr. 43 (1), 187–204. http://dx.doi.org/10.1175/JPO-D-12-081.1.
- Lahaye, N., Gula, J., Thurnherr, A.M., Reverdin, G., Bouruet-Aubertot, P., Roullet, G., 2019. Deep currents in the rift valley of the north mid-Atlantic ridge. Front. Mar. Sci. 6, 597. http://dx.doi.org/10.3389/fmars.2019.00597.
- Lisniowski, M.A., 2020. Caracterização de potenciais habitats bentônicos na elevação do Rio Grande (Ph.D. thesis). Universidade Federal Fluminense, URL: https://rigeo. cprm.gov.br/handle/doc/21753.
- Lisniowski, M.A., Harlamov, V., Frazão, E.P., Pessanha, I.B., Neto, A.A., 2017. Sediment waves on the Rio Grande Rise. In: 2017 IEEE/OES Acoustics in Underwater Geosciences Symposium (RIO Acoustics). IEEE, pp. 1–5. http://dx.doi.org/10.1109/ RIOAcoustics.2017.8349731.
- Locarnini, M., Mishonov, A., Baranova, O., Boyer, T., Zweng, M., Garcia, H., Seidov, D., Weathers, K., Paver, C., Smolyar, I., et al., 2018. World Ocean Atlas 2018, Volume 1: Temperature.
- Luko, C., Silveira, I., Simoes-Sousa, I., Araujo, J., Tandon, A., 2021. Revisiting the Atlantic South Equatorial Current. J. Geophys. Res.: Oceans 126 (7), e2021JC017387. http://dx.doi.org/10.1029/2021JC017387.
- Mellor, G.L., 2004. Users guide for a three dimensional, primitive equation, numerical ocean model. Citeseer
- Montserrat, F., Guilhon, M., Corrêa, P.V.F., Bergo, N.M., Signori, C.N., Tura, P.M., de los Santos Maly, M., Moura, D., Jovane, L., Pellizari, V., et al., 2019. Deep-sea mining on the Rio Grande Rise (Southwestern Atlantic): A review on environmental baseline, ecosystem services and potential impacts. Deep Sea Res. Part I: Oceanogr. Res. Pap. 145, 31–58. http://dx.doi.org/10.1016/j.dsr.2018.12.007.
- Nagai, T., Hibiya, T., 2015. Internal tides and associated vertical mixing in the Indonesian Archipelago. J. Geophys. Res.: Oceans 120 (5), 3373–3390. http://dx. doi.org/10.1002/2014/C010592.
- Nash, J.D., Alford, M.H., Kunze, E., 2005. Estimating internal wave energy fluxes in the ocean. J. Atmos. Ocean. Technol. 22 (10), 1551–1570. http://dx.doi.org/10. 1175/JTECH1784.1.
- Nikurashin, M., Legg, S., 2011. A mechanism for local dissipation of internal tides generated at rough topography. J. Phys. Oceanogr. 41 (2), 378–395. http://dx.doi. org/10.1175/2010JPO4522.1.
- Niwa, Y., Hibiya, T., 2004. Three-dimensional numerical simulation of M2 internal tides in the East China Sea. J. Geophys. Res.: Oceans 109 (C4), http://dx.doi.org/ 10.1029/2003JC001923.
- Paiva, A.M., Daher, V.B., Costa, V.S., Camargo, S.S., Mill, G.N., Gabioux, M., Alvarenga, J.B., 2018. Internal tide generation at the Vitória-Trindade Ridge, South Atlantic Ocean. J. Geophys. Res.: Oceans 123 (8), 5150–5159. http://dx.doi.org/10.1029/2017JC013725.
- Pawlowicz, R., Beardsley, B., Lentz, S., 2002. Classical tidal harmonic analysis including error estimates in MATLAB using T_TIDE. Comput. Geosci. 28 (8), 929–937. http://dx.doi.org/10.1016/S0098-3004(02)00013-4.
- Pereira, A.F., Castro, B.M., 2007. Internal tides in the southwestern Atlantic off Brazil: observations and numerical modeling. J. Phys. Oceanogr. 37 (6), 1512–1526. http://dx.doi.org/10.1175/JPO3075.1.
- Pereira, A., Castro, B., Calado, L., da Silveira, I., 2007. Numerical simulation of M2 internal tides in the South Brazil Bight and their interaction with the Brazil Current. J. Geophys. Res.: Oceans 112 (C4), http://dx.doi.org/10.1029/2006JC003673.
- Peterson, R.G., Stramma, L., 1991. Upper-level circulation in the South Atlantic Ocean.

 Prog. Oceanogr. 26 (1), 1–73. http://dx.doi.org/10.1016/0079-6611(91)90006-8.
- Praxedes, A.G.P., de Castro, D.L., Torres, L.C., Gambôa, L.A.P., Hackspacher, P.C., 2019.
 New insights of the tectonic and sedimentary evolution of the Rio Grande Rise,
 South Atlantic Ocean. Mar. Pet. Geol. 110, 335–346. http://dx.doi.org/10.1016/j.
 marnetgeo.2019.07.035.
- Rocha, C.B., da Silveira, I.C., Castro, B.M., Lima, J.A.M., 2014. Vertical structure, energetics, and dynamics of the Brazil Current System at 22 S-28 S. J. Geophys. Res.: Oceans 119 (1), 52-69. http://dx.doi.org/10.1002/2013JC009143.

- Rodrigues, R.R., Rothstein, L.M., Wimbush, M., 2007. Seasonal variability of the South Equatorial Current bifurcation in the Atlantic Ocean: A numerical study. J. Phys. Oceanogr. 37 (1), 16–30. http://dx.doi.org/10.1175/JPO2983.1.
- Shchepetkin, A.F., McWilliams, J.C., 2005. The regional oceanic modeling system (ROMS): a split-explicit, free-surface, topography-following-coordinate oceanic model. Ocean Model. 9 (4), 347–404. http://dx.doi.org/10.1016/j.ocemod.2004.
- Silva, A.P., 2021. Brazil advances over the Area: The inclusion of the Rio Grande Rise within the Brazilian outer continental shelf and its consequences for other states and for the common heritage of mankind. Mar. Policy 125, 104399. http: //dx.doi.org/10.1016/j.marpol.2021.104399.
- Simoes-Sousa, I.T., Silveira, I.C.A., Tandon, A., Flierl, G.R., Ribeiro, C.H., Martins, R.P., 2021. The Barreirinhas Eddies: Stable energetic anticyclones in the near-equatorial South Atlantic. Front. Mar. Sci. http://dx.doi.org/10.3389/fmars.2021.617011.
- Stashchuk, N., Vlasenko, V., 2017. Bottom trapped internal waves over the Malin Sea continental slope. Deep Sea Res. Part I: Oceanogr. Res. Pap. 119, 68–80. http://dx.doi.org/10.1016/j.dsr.2016.11.007.
- Stramma, L., England, M., 1999. On the water masses and mean circulation of the South Atlantic Ocean. J. Geophys. Res.: Oceans 104 (C9), 20863–20883. http: //dx.doi.org/10.1029/1999JC900139.
- Subeesh, M., Unnikrishnan, A., Francis, P., 2021. Generation, propagation and dissipation of internal tides on the continental shelf and slope off the west coast of India. Cont. Shelf Res. 214, 104321. http://dx.doi.org/10.1016/j.csr.2020.104321.
- Thurnherr, A., St. Laurent, L., Speer, K., Toole, J., Ledwell, J., 2005. Mixing associated with sills in a canyon on the midocean ridge flank. J. Phys. Oceanogr. 35 (8), 1370–1381. http://dx.doi.org/10.1175/JPO2773.1.
- Toffoli, M.R., Paiva, A.M., Costa, V.S., Mill, G.N., 2023. Observations of internal tides at the Vitória-Trindade Ridge, South Atlantic Ocean. J. Geophys. Res.: Oceans 128 (9), e2022JC019606. http://dx.doi.org/10.1029/2022JC019606.
- Vic, C., Gula, J., Roullet, G., Pradillon, F., 2018. Dispersion of deep-sea hydrothermal vent effluents and larvae by submesoscale and tidal currents. Deep Sea Res. Part I: Oceanogr. Res. Pap. 133, 1–18. http://dx.doi.org/10.1016/j.dsr.2018.01.001.

- Vic, C., Naveira Garabato, A.C., Green, J.M., Waterhouse, A.F., Zhao, Z., Melet, A., de Lavergne, C., Buijsman, M.C., Stephenson, G.R., 2019. Deep-ocean mixing driven by small-scale internal tides. Nat. Commun. 10 (1), 2099. http://dx.doi.org/10.1038/s41467-019-10149-5.
- Vlasenko, V., Stashchuk, N., Inall, M.E., Hopkins, J.E., 2014. Tidal energy conversion in a global hot spot: On the 3-D dynamics of baroclinic tides at the Celtic Sea shelf break. J. Geophys. Res.: Oceans 119 (6), 3249–3265. http://dx.doi.org/10.1002/ 2013JC009708.
- Vlasenko, V., Stashchuk, N., Inall, M.E., Porter, M., Aleynik, D., 2016. Focusing of baroclinic tidal energy in a canyon. J. Geophys. Res.: Oceans 121 (4), 2824–2840. http://dx.doi.org/10.1002/2015JC011314.
- Vlasenko, V., Stashchuk, N., Nimmo-Smith, W.A.M., 2018. Three-dimensional dynamics of baroclinic tides over a seamount. J. Geophys. Res.: Oceans 123 (2), 1263–1285. http://dx.doi.org/10.1002/2017JC013287.
- Wang, X., Peng, S., Liu, Z., Huang, R.X., Qian, Y.-K., Li, Y., 2016. Tidal mixing in the South China Sea: An estimate based on the internal tide energetics. J. Phys. Oceanogr. 46 (1), 107–124. http://dx.doi.org/10.1175/JPO-D-15-0082.1.
- Wright, D.G., Loder, J.W., 1985. A depth-dependent study of the topographic rectification of tidal currents. Geophys. Astrophys. Fluid Dyn. 31 (3–4), 169–220. http://dx.doi.org/10.1080/03091928508219269.
- Xu, G., Lavelle, J., 2017. Circulation, hydrography, and transport over the summit of Axial Seamount, a deep volcano in the Northeast Pacific. J. Geophys. Res.: Oceans 122 (7), 5404–5422. http://dx.doi.org/10.1002/2016JC012464.
- Yeo, I., Howarth, S., Spearman, J., Cooper, A., Crossouard, N., Taylor, J., Turnbull, M., Murton, B., 2019. Distribution of and hydrographic controls on ferromanganese crusts: tropic seamount, Atlantic. Ore Geol. Rev. 114, 103131. http://dx.doi.org/ 10.1016/j.oregeorev.2019.103131.
- Zilberman, N., Becker, J., Merrifield, M., Carter, G., 2009. Model estimates of M2 internal tide generation over Mid-Atlantic Ridge topography. J. Phys. Oceanogr. 39 (10), 2635–2651. http://dx.doi.org/10.1175/2008JPO4136.1.
- Zweng, M., Seidov, D., Boyer, T., Locarnini, M., Garcia, H., Mishonov, A., Baranova, O., Weathers, K., Paver, C., Smolyar, I., et al., 2019. World Ocean Atlas 2018, Volume 2: Salinity.